Journal of Photonics for Energy

PhotonicsforEnergy.SPIEDigitalLibrary.org

Influence of hBN orientation on the near-field radiative heat transfer between graphene/hBN heterostructures

Xiaohu Wu
Ceji Fu
Zhuomin Zhang

SPIE.

Xiaohu Wu, Ceji Fu, Zhuomin Zhang, "Influence of hBN orientation on the near-field radiative heat transfer between graphene/hBN heterostructures," *J. Photon. Energy* **9**(3), 032702 (2018), doi: 10.1117/1.JPE.9.032702.

Influence of hBN orientation on the near-field radiative heat transfer between graphene/hBN heterostructures

Xiaohu Wu,[a,b] Ceji Fu,[a,*] and Zhuomin Zhang[b,*]
[a]Peking University, College of Engineering, LTCS and Department of Mechanics and Engineering Science, Beijing, China
[b]Georgia Institute of Technology, George W. Woodruff School of Mechanical Engineering, Atlanta, Georgia, United States

Abstract. The influence of the optic axis orientation of hexagonal boron nitride (hBN) on the near-field radiative heat transfer between hBN slabs as well as between graphene/hBN heterostructures is studied. A modified 4×4 transfer matrix method is employed to calculate the near-field radiative heat flux (NFRHF) between the media. The numerical results show that the NFRHF will decrease when the optic axis of hBN is tilted off the direction of the energy flow for bare hBN slabs. The reason is that hyperbolic phonon polaritons excited in the hyperbolic bands of type I are largely suppressed for tilted optic axis, though surface phonon polaritons can be excited in the hyperbolic bands. On the contrary, the NFRHF between two graphene/hBN heterostructures is affected by the coupling of SPPs excited at the vacuum/graphene interface with those at the graphene/hBN interface and the formation of a hybrid mode, by which the NFRHF is maximum when the hBN slabs are arranged with strong in-plane anisotropy of the surface. The results obtained in this work may provide a promising way for manipulating near-field radiative heat transfer between anisotropic materials. © *2018 Society of Photo-Optical Instrumentation Engineers (SPIE)* [DOI: 10.1117/1.JPE.9.032702]

Keywords: near-field; thermal radiation; hexagonal boron nitride; graphene/hexagonal boron nitride heterostructure; optic axis.

Paper 18108SS received Sep. 25, 2018; accepted for publication Nov. 13, 2018; published online Dec. 4, 2018.

1 Introduction

It is well known that the radiative heat flux between two objects in the near-field regime can be much larger than that predicted with the Stefan–Boltzmann law owing to the contribution from evanescent waves.[1–4] Especially, the power flux can exceed the blackbody limit by several orders in magnitude if surface polaritons or hyperbolic modes can be excited.[5–10] The enhanced radiative heat transfer in the near field has been shown to have promising applications in therophotovoltaics,[11–13] thermal rectification,[14] noncontact refrigeration,[15] and thermal transistor,[16] to name a few.

Various materials and structures have been proposed to obtain a huge near-field radiative heat transfer, such as polar materials,[17,18] doped silicon,[19–21] hyperbolic materials,[22–26] metasurfaces,[27,28] magnetic-optical materials,[29,30] and magneto-dielectric uniaxial anisotropic media.[31–33] A large number of artificial hyperbolic metamaterials have been investigated for enhancing near-field radiative heat transfer due to their hyperbolic dispersion property for electromagnetic (EM) wave propagation, which originates from one of the principal components of their permittivity tensor having an opposite sign to the other two principal components. However, when the tangential wavevector component is larger than π/P (P is the period of the artificial metamaterial), the hyperbolic dispersion will not hold any more.[34] Therefore, there is period limitation for artificial metamaterial. In contrast, for natural hyperbolic material, such as hexagonal boron nitride (hBN) as the lattice constant is on the order of subnanometer, such limitation on the wavevector for near-field thermal radiation is negligible. hBN has attracted much attention in the near-field

*Address all correspondence to: Ceji Fu, E-mail: cjfu@pku.edu.cn; Zhuomin Zhang E-mail: zhuomin.zhang@me.gatech.edu

radiative heat transfer research recently. Zhao et al.[35,36] and Shi et al.[37] studied the enhanced near-field radiative heat transfer between multilayer graphene/hBN heterostructures. In their work, the optic axis of hBN is considered to be along the energy flow. Liu and Xuan[38] studied the near-field radiative transfer between two hBN films when the optic axis of the hBN film is perpendicular to the direction of the energy flow. However, the situation becomes much more complicated if the optic axis of hBN is neither parallel nor perpendicular to the energy flow direction. Nevertheless, the influence of the optic axis orientation of hBN on the near-field radiative heat transfer has not been studied yet.

In the present study, we numerically investigate the effect of optic axis orientation of hBN on the near-field radiative heat transfer between two planar hBN slabs and between two graphene/hBN heterostructures. We have developed a modified 4×4 transfer matrix method that circumvents the vector projection operation with the traditional 4×4 transfer matrix method[39] and combined it with the fluctuation-dissipation theorem (FDT)[9] to calculate the near-field radiative heat flux (NFRHF). By adopting the enhanced transmittance matrix approach,[40] this modified 4×4 transfer matrix method is capable of calculating the NFRHF between multilayered structures while avoiding the problem of numerical overflow when dealing with evanescent waves. The effect of optic axis orientation on the NFRHF for both bare hBN slabs and graphene/hBN heterostructures is studied, and the underlying physical mechanisms are elucidated with the help of dispersion relations of surface and volume modes.

2 Theory and Methods

As an anisotropic material, the optical response of hBN is related to the orientation of its optic axis. In this paper, we studied the near-field radiative heat transfer between a planar emitter and a planar receiver separated by a vacuum gap as shown in Fig. 1. The structures of the emitter and the receiver are essentially the same, which consist of bare hBN slabs or graphene-covered hBN slabs. For convenience, the optic axis of hBN is considered in the $x-z$ plane of the coordinate system xyz and is tilted off the z-axis by angles of α_1 and α_2 for the emitter and the receiver, respectively. In addition, the vacuum gap width and the thickness of hBN are denoted by d and h, respectively.

When the optic axis of hBN is along the z-axis of the coordinate system xyz, its permittivity tensor can be expressed as[35–38]

$$\boldsymbol{\varepsilon}=\begin{pmatrix}\varepsilon_{\perp} & 0 & 0\\ 0 & \varepsilon_{\perp} & 0\\ 0 & 0 & \varepsilon_{\parallel}\end{pmatrix},\quad \varepsilon_m(\omega)=\varepsilon_{\infty,m}\left(1+\frac{\omega_{LO,m}^2-\omega_{TO,m}^2}{\omega_{TO,m}^2-\omega^2+j\omega\Gamma_m}\right), \tag{1}$$

where $m=\perp,\parallel$ indicates the component perpendicular or parallel to the optic axis and ω is the angular frequency. The other parameters are $\omega_{TO,\perp}=2.58\times10^{14}$ rad/s, $\omega_{TO,\parallel}=1.47\times10^{14}$ rad/s, $\omega_{LO,\perp}=3.03\times10^{14}$ rad/s, $\omega_{LO,\parallel}=1.56\times10^{14}$ rad/s, $\varepsilon_{\infty,\perp}=4.87$, $\varepsilon_{\infty,\parallel}=2.95$, $\Gamma_{\perp}=9.42\times10^{11}$ rad/s, and $\Gamma_{\parallel}=7.54\times10^{11}$ rad/s. One can easily determine from Eq. (1) that the dispersion relation for EM waves propagating in hBN exhibits the property of hyperbolicity in two frequency bands: the one between 1.47×10^{14} and 1.56×10^{14} rad/s is called the hyperbolic band of type I, where $\varepsilon_{\parallel}<0$ and $\varepsilon_{\perp}>0$; the

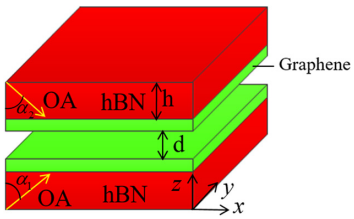

Fig. 1 Schematic of near-field radiative heat transfer between two graphene/hBN heterostructures. The optic axis (OA) of hBN is in the $x-z$ plane and is tilted off the z-axis by an angle.

other one between 2.58×10^{14} rad/s and 3.03×10^{14} is called the hyperbolic band of type II, where $\varepsilon_{||} > 0$ and $\varepsilon_{\perp} < 0$.[37,38] Now if its optic axis is tilted off the z-axis by an angle α in the $x - z$ plane, the permittivity tensor of hBN can be expressed as[41]

$$\boldsymbol{\varepsilon} = \begin{pmatrix} \varepsilon_{\perp}\cos^2\alpha + \varepsilon_{||}\sin^2\alpha & 0 & (\varepsilon_{||} - \varepsilon_{\perp})\sin\alpha\cos\alpha \\ 0 & \varepsilon_{\perp} & 0 \\ (\varepsilon_{||} - \varepsilon_{\perp})\sin\alpha\cos\alpha & 0 & \varepsilon_{\perp}\sin^2\alpha + \varepsilon_{||}\cos^2\alpha \end{pmatrix}. \tag{2}$$

Graphene is modeled as a layer of thickness $\Delta = 0.3$ nm with an effective dielectric function:[36]

$$\varepsilon_{\text{eff}} = 1 - \frac{j\sigma_s}{\varepsilon_0 \omega \Delta}, \tag{3}$$

where ε_0 is the absolute permittivity of vacuum and σ_s is the sheet conductivity that includes the contributions from both the interband and intraband transitions. In the mid- and far-infrared region, σ_s is dominated by the intraband transitions and can be approximately written as[36]

$$\sigma_s = \frac{e^2\mu}{\pi\hbar^2}\frac{\tau}{1 + j\omega\tau}, \tag{4}$$

where e is the electron charge, $\hbar$ is the reduced Planck constant, τ is the relaxation time, and μ is the chemical potential.

Based on the fluctuation-dissipation theorem and the reciprocity of the dyadic green function, the NFRHF between anisotropic media can be expressed as[38,42]

$$Q = \frac{1}{8\pi^3}\int_0^{\infty}[\Theta(\omega, T_1) - \Theta(\omega, T_2)]\mathrm{d}\omega \int_0^{2\pi}\int_0^{\infty}\xi(\omega, \beta, \phi)\beta\mathrm{d}\beta\mathrm{d}\phi, \tag{5}$$

where $\Theta(\omega, T) = \hbar\omega/(e^{\hbar\omega/k_B T} - 1)$ is the average energy of a Planck oscillator, ϕ is the azimuth angle, and $\xi(\omega, \beta, \phi)$ is called the energy transmission coefficient or the phonon tunneling probability, which can be expressed as[42]

$$\xi(\omega, \beta, \phi) = \begin{cases} \mathrm{Tr}[(\mathbf{I} - \mathbf{R}_2^*\mathbf{R}_2 - \mathbf{T}_2^*\mathbf{T}_2)\mathbf{D}(\mathbf{I} - \mathbf{R}_1^*\mathbf{R}_1 - \mathbf{T}_1^*\mathbf{T}_1)\mathbf{D}^*], & \beta < k_0 \\ \mathrm{Tr}[(\mathbf{R}_2^* - \mathbf{R}_2)\mathbf{D}(\mathbf{R}_1 - \mathbf{R}_1^*)\mathbf{D}^*]e^{-2|k_z|d}, & \beta > k_0 \end{cases}, \tag{6}$$

where $k_0 = \omega/c$ is the wavevector in vacuum with c the speed of light in vacuum. β is the wavevector component parallel to the $x - y$ plane. $k_z = \sqrt{k_0^2 - \beta^2}$ is the wavevector component along the z-axis in vacuum. Note that the asterisk denotes conjugate transpose, and $\mathrm{Tr}(\cdot)$ takes the trace of a matrix. $\mathbf{I}$ is a 2×2 unit matrix and

$$\mathbf{R}_{1,2} = \begin{bmatrix} r_{ss}^{(1,2)} & r_{sp}^{(1,2)} \\ r_{ps}^{(1,2)} & r_{pp}^{(1,2)} \end{bmatrix}, \quad \mathbf{T}_{1,2} = \begin{bmatrix} t_{ss}^{(1,2)} & t_{sp}^{(1,2)} \\ t_{ps}^{(1,2)} & t_{pp}^{(1,2)} \end{bmatrix}, \tag{7}$$

are the matrices that include the reflection and transmission coefficients for incident s- and p-polarized plane waves from vacuum to the emitter or the receiver, respectively. The first and second letters of the subscript in each coefficient denote the polarization state of incident and reflected (transmitted) waves, respectively. These coefficients can be obtained using a modified 4×4 transfer matrix method (see Sec. 5 Appendix for detailed description). Note that $\mathbf{T} = 0$ if the incidence is on a semi-infinite medium. The matrix $\mathbf{D}$ is given as $\mathbf{D} = (\mathbf{I} - \mathbf{R}_1\mathbf{R}_2 e^{-2jk_z d})^{-1}$.

3 Results and Discussion

In this work, we set the emitter temperature $T_1 = 300$ K, the receiver temperature $T_2 = 0$ K, $d = 20$ nm, $\mu = 0.37$ eV, and $\tau = 10^{-13}$ s. In addition, the tilting angles α_1 and α_2 are first assumed as $\alpha_1 = \alpha_2 = \alpha$. Four cases are investigated and compared with each other: bulk

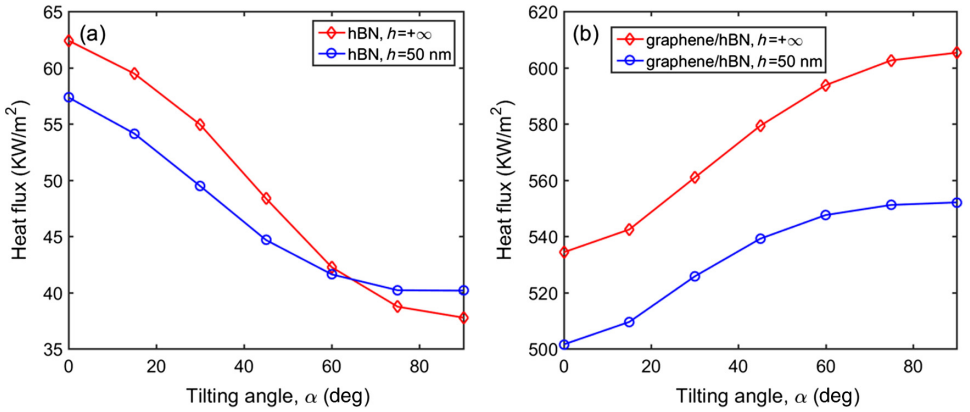

Fig. 2 NFRHF between (a) two bare hBN slabs and (b) two graphene-covered hBN slabs as a function of the tilting angle of hBN optic axis.

hBN, hBN slab with thickness of 50 nm, graphene-covered bulk hBN, and graphene-covered hBN slab with thickness of 50 nm. The NFRHF as a function of the tilting angle is shown in Fig. 2 for the four cases. One can see from Fig. 2(a) that the NFRHF between two bulk hBN slabs (i.e., $h = +\infty$) is larger than that between two hBN slabs of $h = 50$ nm at $\alpha = 0$ deg. The heat fluxes of both cases decrease with the tilting angle, but the decrease is faster for the former than for the latter such that the heat flux of the former becomes smaller than that of the latter when α is larger than 65 deg. On the other hand, as shown in Fig. 2(b), the NFRHF between two graphene/hBN heterostructures of $h = +\infty$ is also larger than that between two graphene/hBN heterostructures of $h = 50$ nm. But the heat fluxes of these two cases both increase with the tilting angle, and the increase is faster for the former than for the latter. In addition, one can find by comparing Fig. 2(b) with Fig. 2(a) that the NFRHF between two graphene/hBN heterostructures is larger than that between two bare hBN slabs by around one order of magnitude.

To elucidate the effect of the tilting angle of the hBN optic axis on the near-field radiative heat transfer between the two media, the corresponding spectral NFRHF is shown in Fig. 3 for α equal to 0 deg, 45 deg, and 90 deg, respectively. One can see that the NFRHF between two bare hBN slabs is mainly contributed from the two hyperbolic bands as shown in Figs. 3(a) and 3(b), respectively. For ease of analysis, the dispersion relation for EM wave propagating in bulk hBN is given below as[22,23]

$$\frac{k_{\perp}^2}{\varepsilon_{||}} + \frac{k_{||}^2}{\varepsilon_{\perp}} = \left(\frac{\omega}{c}\right)^2, \tag{8}$$

where $k_{\perp}$ and $k_{||}$ denote, respectively, the wavevector component perpendicular and parallel to the optic axis. Note that the expression in Eq. (8) is in a different form from that in Refs. 22 and 23 because $\varepsilon_{\perp}$ and $\varepsilon_{||}$ are defined differently from those in Refs. 22 and 23. Note also that $k_{||} = k_z$ and $k_{\perp}^2 = k_x^2 + k_y^2$ when the optic axis is in the z-direction, whereas $k_{||} = k_x$ and $k_{\perp}^2 = k_y^2 + k_z^2$ when the optic axis is in the x-direction, corresponding to the tilting angle α equal respectively to 0 deg and 90 deg in this work. In the two hyperbolic bands with opposite signs of $\varepsilon_{\perp}$ and $\varepsilon_{||}$, the solutions to Eq. (8) for a given frequency are three-dimensional (3-D) open hyperboloids. As a consequence, thermal emission waves in hBN are propagating waves for $k_{\perp}$ and $k_{||}$ far exceeding k_0, which provides more channels for photon tunneling and thus greatly enhances the NFRHF compared with that in the other frequency bands. These channels for the enhanced NFRHF have previously been termed as hyperbolic phonon polaritons (HPPs)[35,36,43] or hyperbolic modes.[22,23] But the heat flux contributed from these two hyperbolic bands is sensitive to the tilting angle of the optic axis. For two bulk hBN slabs, the heat flux contributed from the hyperbolic bands of types I and II is 43.18 and 17.27 kW/m^2, respectively, when the tilting angle is 0 deg. The contributions from these two hyperbolic bands are 22.08 and 24.59 kW/m^2 when the tilting

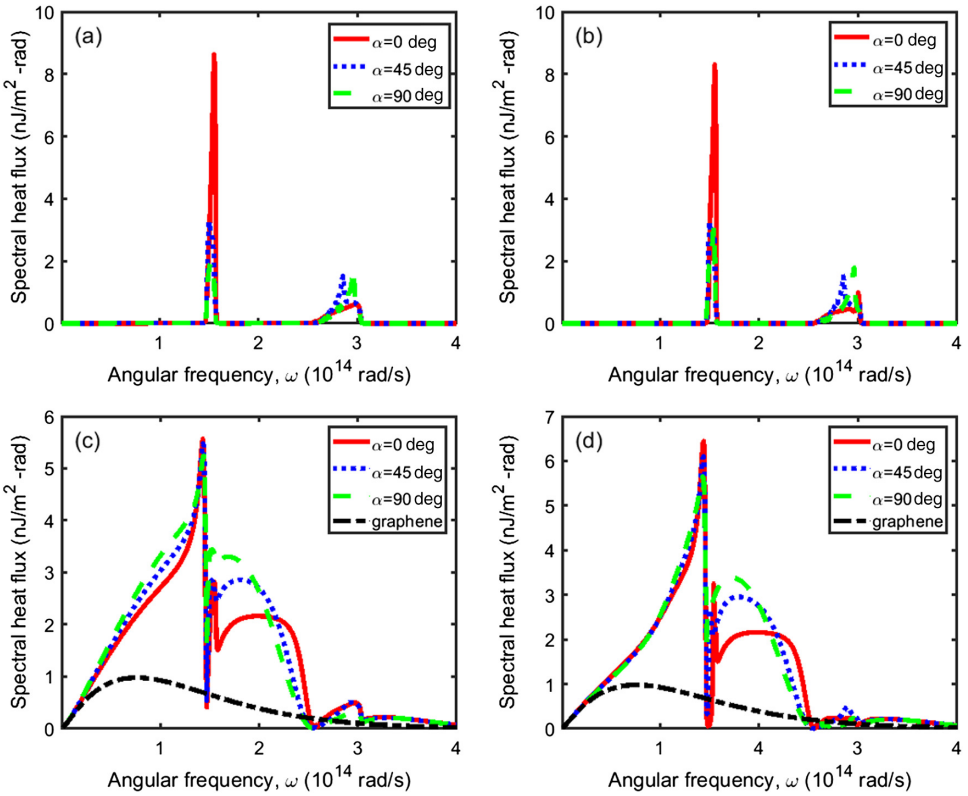

Fig. 3 Spectral NFRHF between (a) bulk hBN slabs, (b) hBN slabs with thickness of 50 nm, (c) graphene-covered bulk hBN slabs, and (d) graphene-covered hBN slabs with thickness of 50 nm.

angle is 45 deg and are 14.25 and 21.92 kW/m^2 when the tilting angle is 90 deg. Therefore, the heat transfer contributed from the hyperbolic band of type I decreases dramatically with the tilting angle while that contributed from the hyperbolic band of type II does not change much. There is a significant decrease in the heat flux around $\omega = 1.55 \times 10^{14}$ rad/s as the tilting angle increases. In addition, there appears a peak at $\omega = 2.85 \times 10^{14}$ rad/s for $\alpha = 45$ deg and at $\omega = 2.96 \times 10^{14}$ rad/s for $\alpha = 90$ deg. However, for the graphene/hBN heterostructures, the spectral NFRHF is greatly enhanced in two much wider frequency bands below and between the two hyperbolic bands, as shown in Figs. 3(c) and 3(d). This is due to excitation of surface plasmon polaritons (SPPs) at the vacuum/graphene and graphene/hBN interfaces. Therefore, the NFRHF between the graphene/hBN heterostructures is dominated by SPPs, instead of HPPs. In addition, the excited SPPs can couple with HPPs, resulting in the formation of a hybrid mode, to be discussed below. For comparison, the NFRHF between two free standing graphene sheets is also shown in Figs. 3(c) and 3(d), which is much lower than that between the graphene/hBN heterostructures. Note that from Fig. 3, not much change is found for the results when the hBN slab thickness h is changed from 50 nm to ∞, which comes from the fact that for $d_2 = 20$ nm, a thickness of 50 nm is almost large enough for a hBN slab to be treated as bulk for near-field radiative heat transfer.

The underlying mechanism of the effect of the tilted optic axis of hBN can be better understood by presenting the energy transmission coefficient ξ in the $k_x - k_y$ plane. Figures 4(a) and 4(b) show the energy transmission coefficient ξ between two bulk hBN slabs varying with the wavevector components k_x and k_y at $\omega = 1.55 \times 10^{14}$ rad/s when the tilting angle α is equal to 0 deg and 90 deg, respectively. When α is equal to 0 deg, the optic axis is along the z-axis and the permittivity tensor of hBN possesses rotational symmetry in the $x - y$ plane, which results in the solutions to Eq. (8) possessing rotational symmetry in the $k_x - k_y$ plane. Hence, the energy transmission coefficient also exhibits rotational symmetry in the $k_x - k_y$ plane. As shown in Fig. 4(a), the bright circular region centered at the origin and with radius far exceeding k_0 indicates

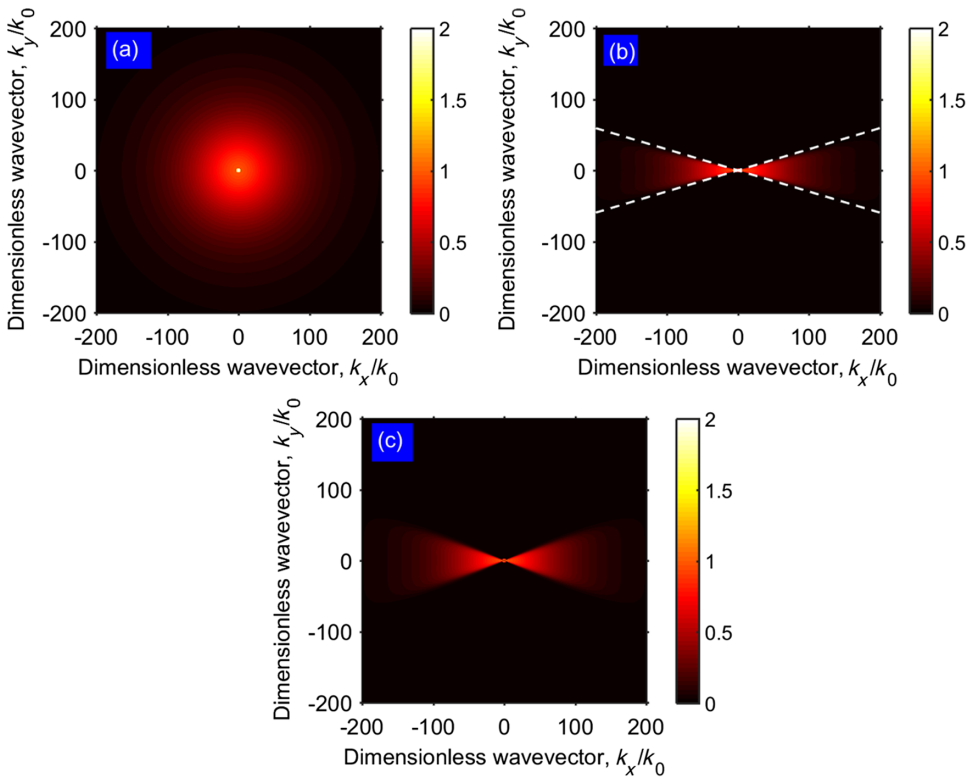

Fig. 4 Energy transmission coefficient between two bulk hBN slabs varying with wavevector components k_x and k_y at 1.55×10^{14} rad/s: (a) $\alpha = 0$ deg, (b) $\alpha = 90$ deg, and (c) $\alpha = 45$ deg.

excitation of HPPs in the hBN slabs, which greatly enhances the spectral NFRHF between the slabs. However, when α is equal to 90 deg, the optic axis is along the x-axis and the permittivity tensor of hBN has no rotational symmetry in the $x - y$ plane in this case. In fact, the projected HPP isofrequency surface in the $k_x - k_y$ plane is the region bounded by the hyperbolas corresponding to $k_z = 0$ in Eq. (8). In addition, it has been shown that hyperbolic surface phonon polaritons (HSPhPs), which are resonant modes confined on the surface of hBN, can be excited in this case due to the strong anisotropy of the surface, i.e., opposite signs of $\varepsilon_\perp$ and $\varepsilon_{||}$.[38,43] The dispersion of HSPhPs can, when the values of k_x and k_y are far exceeding the wavevector k_0, be written concisely as[38]

$$k_x^2(\varepsilon_{||}\varepsilon_\perp - \varepsilon_d^2) + k_y^2(\varepsilon_\perp^2 - \varepsilon_d^2) = \varepsilon_{||}\varepsilon_\perp^2 \frac{\omega^2}{c^2}, \tag{9}$$

where ε_d denotes the dielectric function of the medium adjacent to hBN and $\varepsilon_d = 1$ for vacuum. At $\omega = 1.55 \times 10^{14}$ rad/s, $\varepsilon_\perp = 7.7707 - 0.0099\,j$ and $\varepsilon_{||} = -0.5455 - 0.1696j$, which makes that the relations $1 - \varepsilon_\perp \varepsilon_{||} > 0$ and $1 - \varepsilon_\perp^2 < 0$, can be satisfied when neglecting the imaginary parts of $\varepsilon_\perp$ and $\varepsilon_{||}$. Therefore, the dispersion in Eq. (9) is hyperbolic. In this case, the asymptotes of the HSPhP dispersion curves in the $k_x - k_y$ plane can be expressed as

$$\frac{k_y}{k_x} = \pm\sqrt{\frac{\varepsilon_d^2 - \varepsilon_{||}\varepsilon_\perp}{\varepsilon_\perp^2 - \varepsilon_d^2}}, \tag{10}$$

and those of the hyperbolas corresponding to $k_z = 0$ in Eq. (8) are given as

$$\frac{k_y}{k_x} = \pm\sqrt{-\frac{\varepsilon_{||}}{\varepsilon_\perp}}, \tag{11}$$

assuming $\varepsilon_\perp$ and $\varepsilon_{||}$ are both real numbers. Considering the values of $\varepsilon_\perp$ and $\varepsilon_{||}$ at $\omega = 1.55 \times 10^{14}$ rad/s and noting that $\varepsilon_d = 1$, the square roots on the right-hand sides of Eqs. (10) and (11) are obtained as 0.297 and 0.265, respectively. For comparison, the asymptotes based on Eq. (10) are also added in Fig. 4(b), which are found in excellent agreement with the numerical results. Furthermore, as the bright color is full of the region bounded by these two lines and the slope in Eq. (11) is slightly smaller than that in Eq. (10), it is difficult to discriminate the dispersion contours of HPPs from Fig. 4(b). Enhancement of the radiative heat transfer may, therefore, result from interaction of excited HSPhPs and HPPs. Nevertheless, the enhanced radiative heat transfer in this case is weaker than that due to HPPs alone for $\alpha = 0$ deg, as seen from Fig. 3(a). Shown in Fig. 4(c) are the contours of the energy transmission coefficient for $\alpha = 45$ deg, which are very similar to those in Fig. 4(b) except that the angle between the two lines bounding the bright color region is larger than that in Fig. 4(b). Therefore, we conclude that the enhanced energy transmission between the two hBN slabs for $\alpha = 45$ deg may still result from interaction of excited HSPhPs and HPPs. This is because the projected HPP isofrequency surface in the $k_x - k_y$ plane is still bounded by hyperbolas and HSPhPs can still be excited though they satisfy a dispersion relation in a form different from that in Eq. (9).

The energy transmission coefficient distribution at 2.85×10^{14} rad/s for two bulk hBN slabs is shown in Figs. 5(a) and 5(b) when the tilting angle is 0 deg and 90 deg, respectively. This frequency is within the hyperbolic band of type II, at which $\varepsilon_\perp = -3.6397 - 0.1572j$ and $\varepsilon_{||} = 2.8085 - 0.0005j$. Hence, the bright circular region shown in Fig. 5(a) for $\alpha = 0$ deg is attributed to HPPs. When $\alpha = 90$ deg, HSPhPs can be excited due to the strong anisotropy of the surface. Keep in mind that $\varepsilon_\perp < 0$ and $\varepsilon_{||} > 0$, and $\varepsilon_\perp \varepsilon_{||} - 1 < 0$ and $\varepsilon_\perp^2 - 1 > 0$ when the imaginary parts of $\varepsilon_\perp$ and $\varepsilon_{||}$ are neglected in this case. These inequalities give rise to the HSPhP dispersion curves being hyperbolas with the two focuses on the k_y-axis, which can be determined from Eq. (9). Excitation of HSPhPs is clearly shown in Fig. 5(b) by the hyperbolas with focuses on the k_y-axis. The two dashed lines in this figure also represent the asymptotes of the HSPhPs dispersion curves drawn based on Eq. (10), which are clearly seen to be in excellent agreement

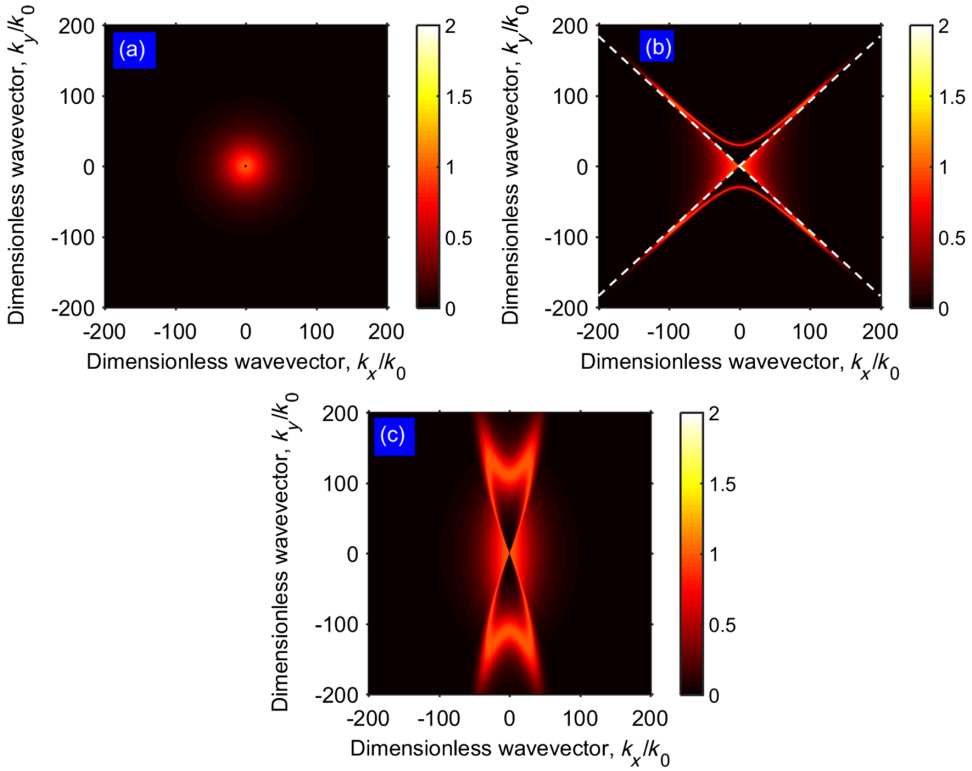

Fig. 5 Energy transmission coefficient between two bulk hBN slabs varying with wavevector components k_x and k_y at 2.85×10^{14} rad/s: (a) $\alpha = 0$ deg, (b) $\alpha = 90$ deg, and (c) $\alpha = 45$ deg.

with the numerical results. Furthermore, the projected HPP isofrequency surface in the $k_x - k_y$ plane is the region bounded by the hyperbolas that extend in the direction of k_x and whose asymptotes are still described by Eq. (11). Enhanced radiative heat transfer due to HPPs is also clearly manifested in Fig. 5(b) by the bright color in the region near the origin. Because the asymptotes of the HPP hyperbolas described by Eq. (11) are close to those of HSPhPs in this case, they are not shown in Fig. 5(b). Plotted in Fig. 5(c) are the contours of the energy transmission coefficient for $\alpha = 45$ deg. Similar results to those in Fig. 5(b) are also found except that the angle between the asymptotes of the HSPhP dispersion curves becomes smaller while that between the asymptotes of the hyperbolas that bound the region for HPPs gets larger. We also attribute the enhanced energy transmission in this case to the interaction of excited HSPhPs and HPPs, which may be the cause that broadens the HSPhP dispersion curves, as shown in Fig. 5(c).

Figures 6(a) and 6(b) show the energy transmission coefficient ξ between two bulk hBN slabs varying with the wavevector components k_x and k_y at $\omega = 2.96 \times 10^{14}$ rad/s, which is also within the hyperbolic band of type II, when the tilting angle α is equal to 0 deg and 90 deg, respectively. At this frequency, $\varepsilon_\perp = -1.0421 - 0.0788j$ and $\varepsilon_{||} = 2.8222 - 0.0004j$. The energy transmission coefficient ξ distribution shown in Fig. 6(a) is similar to that in Fig. 5(a), owing to the contribution from HPPs whose dispersion relation in this case possesses rotational symmetry in the $k_x - k_y$ plane. When $\alpha = 90$ deg, as the relations $1 - \varepsilon_\perp \varepsilon_{||} > 0$ and $1 - \varepsilon_\perp^2 < 0$ are satisfied when neglecting the imaginary parts of $\varepsilon_\perp$ and $\varepsilon_{||}$, HSPhPs can be excited. However, $1 - \varepsilon_\perp^2$ is very close to zero in this case. As such, the dispersion curves solved from Eq. (9) is in a transitional state from hyperbolas to an ellipse, corresponding to a transitional resonant mode from HSPhPs to elliptical surface phonon polaritons (ESPhPs). Figure 6(b) clearly shows this situation, which reveals that the dispersion curves at large $|k_y|$ values have changed from hyperbolas to be flattened and closed. Similar results have also been obtained by Liu and Xuan.[38] In addition, similar to Fig. 5(b), the bright color regions on the two sides of the origin shown in Fig. 6(b) manifest enhanced radiative heat transfer due to HPPs. Note that the

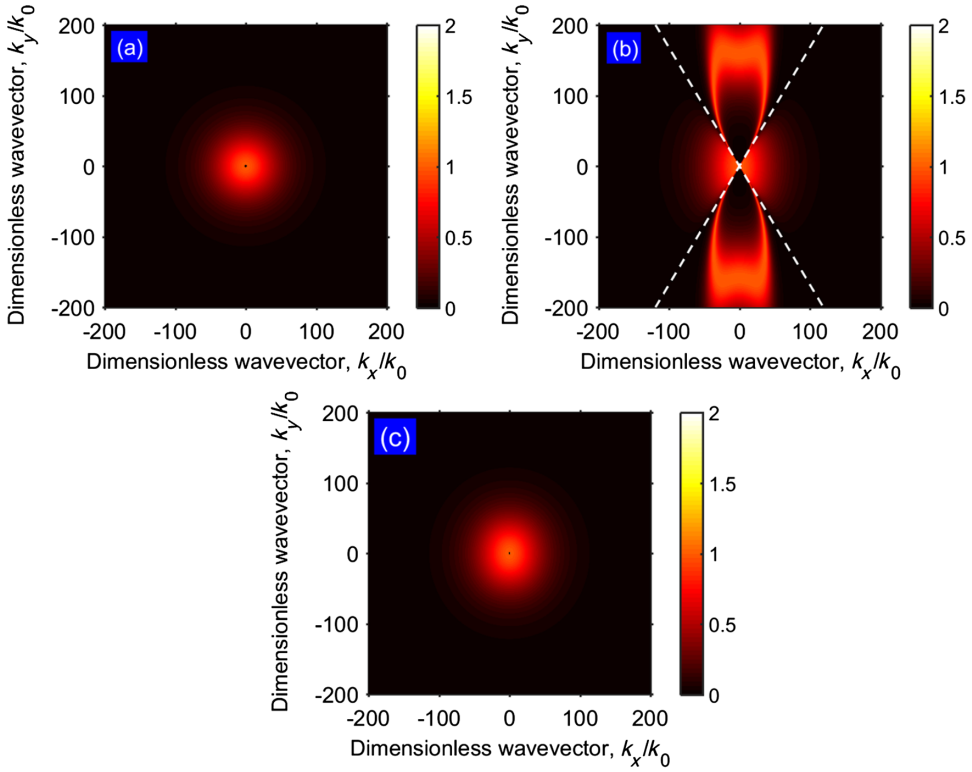

Fig. 6 Energy transmission coefficient between two bulk hBN slabs varying with wavevector components k_x and k_y at 2.96×10^{14} rad/s: (a) $\alpha = 0$ deg, (b) $\alpha = 90$ deg, and (c) $\alpha = 45$ deg.

two dashed lines in Fig. 6(b) represent the asymptotes of the HPP hyperbolas and are drawn based on Eq. (11). Those asymptotes based on Eq. (10) are not shown as in this case, the resonant mode is in a transitional state. Shown in Fig. 6(c) is the energy transmission coefficient ξ distribution for $\alpha = 45$ deg. Interestingly, the bright color region looks very different from that shown in Fig. 6(b). In fact, the bright color region is in an elliptical shape, indicating that the excited surface phonon polaritons are ESPhPs, instead of HSPhPs in this case. Therefore, the enhanced radiative heat transfer is due to the combined effect of ESPhPs and HPPs.

It should be pointed out that the above contour plots are only for the energy transmission coefficient between two bulk hBN slabs. The results for the NFRHF between two hBN slabs of $h = 50$ nm are similar except that the HPP modes are discrete in this case due to wave interference effect in the slabs. More importantly, HSPhPs can be excited on both surfaces of the slab at large tilting angels, the coupling of which can strengthen the radiative heat transfer. As a consequence, the NFRHF between two hBN slabs of $h = 50$ nm can exceed that between two bulk hBN slabs as shown in Fig. 2(a).

The contours of the energy transmission coefficient ξ between two graphene-covered bulk hBN slabs in the $k_x - k_y$ plane and at $\omega = 1.00 \times 10^{14}$ rad/s are shown in Figs. 7(a) and 7(b) for α equal to 0 deg and 90 deg, respectively. It has been shown that SPPs can be excited at vacuum/graphene interface such that the NFRHF between two graphene sheets can be enhanced in a broadband.[36] However, the enhancement is not as significant as shown in Figs. 3(c) and 3(d) because the thickness of graphene is too small. For the case of near-field radiative heat transfer between two graphene-covered bulk hBN slabs, SPPs can be excited at the graphene/hBN interface, besides at the vacuum/graphene interface. Although $\varepsilon_\perp$ and $\varepsilon_{||}$ of hBN are positive at $\omega = 1.00 \times 10^{14}$ rad/s, the real part of the dielectric function of graphene is negative at this frequency. Therefore, the dispersion of SPPs at the graphene/hBN interface can be satisfied, which in the case of $\alpha = 0$ deg can be written as

$$(\varepsilon_d^2 \varepsilon_\perp - \varepsilon_\perp^2 \varepsilon_{||})(k_x^2 + k_y^2) = (\varepsilon_d^2 \varepsilon_\perp \varepsilon_{||} - \varepsilon_\perp^2 \varepsilon_d \varepsilon_{||}) k_0^2, \tag{12}$$

where ε_d represents the dielectric function of graphene as shown in Eq. (3). The dispersion relation shown in Eq. (12) has the property of rotational symmetry in the $k_x - k_y$ plane, so does that of SPPs at the vacuum/graphene interface. The enhanced NFRHF shown in Fig. 7(a), represented by the bright contours of the energy transmission coefficient ξ, is due to the coupling of SPPs excited at the vacuum/graphene interface and at the graphene/hBN interface. Rotational symmetry of the SPP dispersions in the $k_x - k_y$ plane can be clearly observed. In the case that $\alpha = 90$ deg, though the dispersion of SPPs at the vacuum/graphene interface still retains the rotational symmetry in the $k_x - k_y$ plane, the dispersion of SPPs at the graphene/hBN interface, same as in Eq. (9), represents an ellipse with its long axis along k_y as $\varepsilon_\perp = 7.0531 - 0.0036j$ and $\varepsilon_{||} = 3.6763 - 0.0047j$ at $\omega = 1.00 \times 10^{14}$ rad/s. It can be seen clearly in Fig. 7(b) that the inner

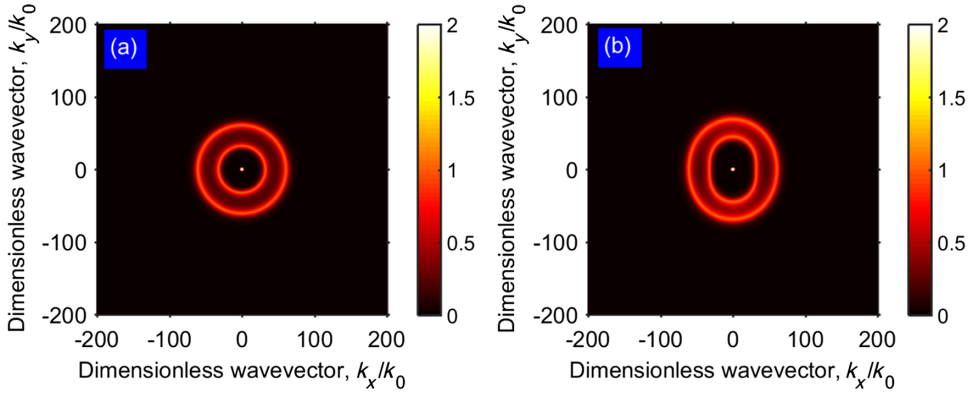

Fig. 7 Energy transmission coefficient between two graphene-covered bulk hBN slabs varying with wavevector components k_x and k_y at 1.0×10^{14} rad/s: (a) $\alpha = 0$ deg and (b) $\alpha = 90$ deg.

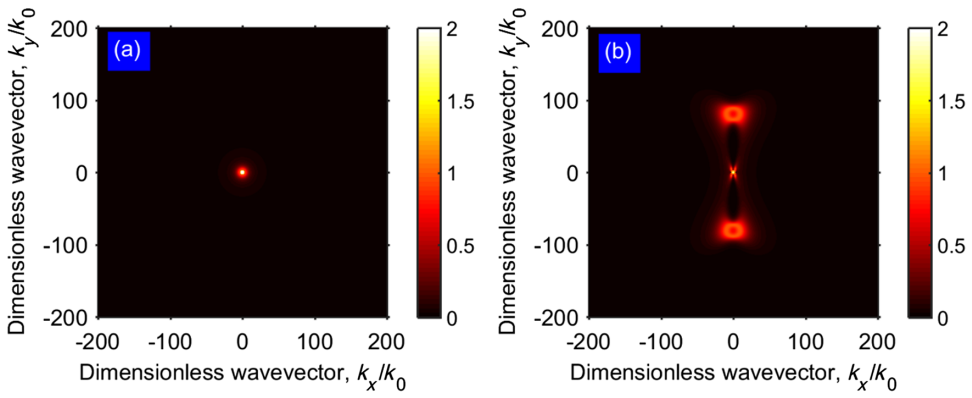

Fig. 8 Contours of the energy transmission coefficient between graphene-covered bulk hBN at 1.47×10^{14} rad/s: (a) $\alpha = 0$ deg and (b) $\alpha = 90$ deg.

ring of the bright contours of ξ indeed exhibits an ellipse with its long axis along k_y, which, due to coupling of SPPs, causes the outer ring to deviate from the circular shape. Change in the dispersion of SPPs at the graphene/hBN interface with the tilting angle α changes the NFRHF as shown in Figs. 3(c) and 3(d), respectively.

Similar mechanisms apply to the enhancement of the NFRHF with the graphene coatings at other frequencies shown in Figs. 3(c) and 3(d) except for the regions close to the hyperbolic bands, where SPPs may strongly interact with HPPs to induce the formation of a hybrid mode. For example, it can be seen from Figs. 3(c) and 3(d) that the radiative heat flux between the graphene/hBN heterostructures at $\omega = 1.47 \times 10^{14}$ rad/s is influenced significantly by the tilting angle of the optic axis of hBN. This frequency is at the edge of the hyperbolic band of type I so that SPPs may interact strongly with HPPs. To see this, we plotted in Figs. 8(a) and 8(b) the energy transmission coefficient distribution at 1.47×10^{14} rad/s when the tilting angle α is 0 deg and 90 deg, respectively. At this frequency, $\varepsilon_\perp = 7.6153 - 0.0084j$ and $\varepsilon_{||} = 8.2826 - 75.7521j$, both $\varepsilon_\perp$ and $\varepsilon_{||}$ are the positive. It can be seen from Fig. 8(a) that for $\alpha = 0$ deg, the bright contours of the energy transmission coefficient ξ are only concentrated around the origin of the $k_x - k_y$ plane, which indicates that the NFRHF is very small in this case and is in accordance with the value shown in Fig. 3(c). This small radiative flux is the result of mode repulsion between excited SPPs and HPPs supported by the structure.[36] But when $\alpha = 90$ deg, the radiative heat flux is significantly enhanced compared with the case of $\alpha = 0$ deg as shown in Fig. 3(c). The corresponding contours of the energy transmission coefficient ξ are shown in Fig. 8(b), which indicate a hybrid mode excitation that comes from the coupling of SPPs and HPPs. In fact, HPPs are bulk modes whose impact is weak if the thickness of the hBN slab is small. We have checked that the distribution of ξ is very similar to that shown in Fig. 7(b) if the thickness of the hBN slab is on the order of 10 nm. As the hBN slab is getting thicker and thicker, the pattern shrinks in the k_x direction and gradually changes to the hybrid mode pattern as shown in Fig. 8(b). The reason is that the HPPs become stronger and stronger as the slab thickness increases, and they eventually can couple with SPPs to form the hybrid mode. Note from Fig. 8(b) that the NFRHF due to HPPs is quite weak, which comes from the fact that the imaginary part of $\varepsilon_{||}$ is very large in this case.

The effect of the tilting angle α on the hybrid mode is further shown in Figs. 9(a) and 9(b), where the energy transmission coefficient ξ between two graphene-covered bulk hBN slabs at $\omega = 1.58 \times 10^{14}$ rad/s is plotted for α equal to 0 deg and 90 deg, respectively. This frequency is beyond but close to the hyperbolic band of type I, at which $\varepsilon_\perp = 7.8360 - 0.0106j$ and $\varepsilon_{||} = 0.4324 - 0.0896j$. Note that $\varepsilon_{||}$ is close to zero in this case. From Fig. 9(a), strong mode repulsion is not seen for $\alpha = 0$ deg, and the distribution pattern of ξ indicates clearly the characteristic of coupled SPPs in this case. When $\alpha = 90$ deg, however, the distribution pattern of ξ is tortured dramatically due to the interaction of SPPs and HPPs and the formation of a hybrid mode. Especially, the ellipse due to the excited SPPs at the graphene/hBN interface is

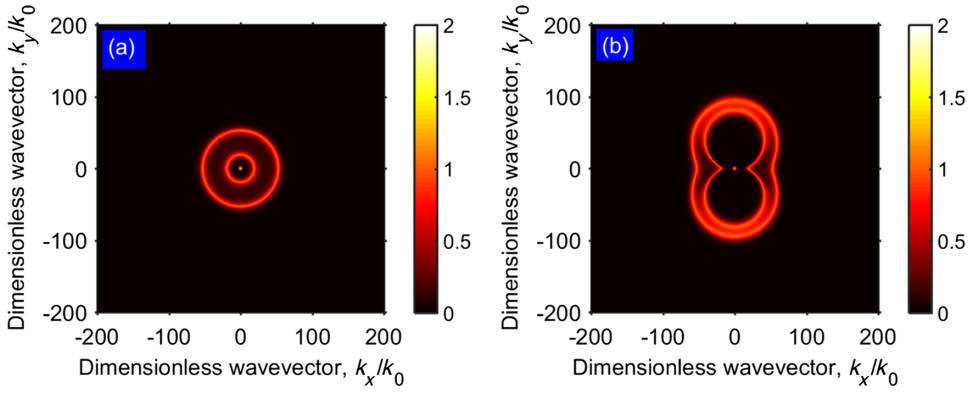

Fig. 9 Contours of the energy transmission coefficient between graphene-covered bulk hBN at 1.58×10^{14} rad/s: (a) $\alpha = 0$ deg and (b) $\alpha = 90$ deg.

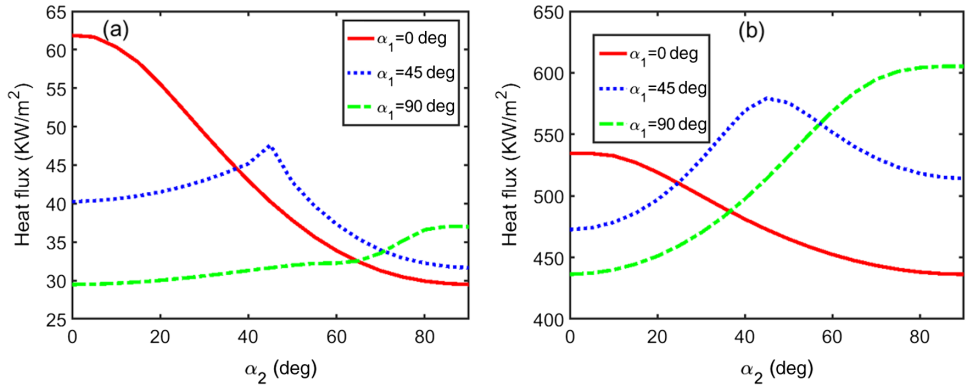

Fig. 10 Effect of different oriented optic axes of hBN on the NFRHF between (a) two bulk hBN slabs and (b) two graphene-covered bulk hBN slabs.

shrunk significantly in the k_x direction and the hyperbolas corresponding to HPPs in the hyperbolic band are clearly seen at small $|k_y|$ values.

Finally, the effect of different tilting angles α_1 and α_2 on the NFRHF is investigated. The results are shown in Figs. 10(a) and 10(b) for the near-field radiative heat transfer between two bulk hBN slabs and between two graphene-covered bulk hBN slabs, respectively. It can be seen that in both cases maximum NFRHF is obtained when the values of α_1 and α_2 are equal. Furthermore, Fig. 10(a) shows that the largest NFRHF between two bulk hBN slabs is obtained when $\alpha_1 = \alpha_2 = 0$ deg, the NFRHF decreases with an increase in the tilting angle. In contrast, the NFRHF between two graphene-covered bulk hBN slabs is the largest when $\alpha_1 = \alpha_2 = 90$ deg, and it decreases with a decrease of the tilting angle. In other words, to enhance the NFRHF between two pure hBN slabs the slabs should be arranged with in-plane isotropy of the surface. But for the graphene-cover hBN slabs, the slabs should be arranged with strong in-plane anisotropy of the surface.

4 Conclusion

We numerically investigated in this work the effect of hBN orientation on the near-field radiative heat transfer between two hBN slabs as well as two graphene/hBN heterostructures. A modified 4×4 transfer matrix method is employed to calculate the NFRHF between anisotropic materials. The numerical results show that the largest NFRHF between two bulk hBN slabs is obtained when the tilting angles of the optic axes are both equal to 0 deg, and the NFRHF decreases with an increase in the tilting angle. In contrast, the NFRHF between two graphene-covered bulk hBN slabs is the largest when the tilting angles of the optic axes are both equal to 90 deg, and it

decreases with a decrease in the tilting angle. The NFRHF will decrease when the optic axis of hBN is tilted off the direction of the energy flow for bare hBN slabs. We showed that HPPs excited in the hyperbolic bands of type I are largely suppressed for tilted optic axis though surface phonon polaritons can be excited in the hyperbolic bands. On the contrary, the NFRHF between two graphene/hBN heterostructures is affected by the coupling of SPPs excited at the vacuum/graphene interface with those at the graphene/hBN interface and the formation of a hybrid mode, by which the NFRHF is maximum when the hBN slabs are arranged with strong in-plane anisotropy of the surface. The results obtained in this work may provide a promising way for manipulating near-field radiative transfer between anisotropic materials.

5 Appendix: The Modified 4 × 4 Transfer Matrix Method

To calculate the near-field radiative heat transfer, it is necessary to calculate the reflection and transmission coefficients at different values of the azimuth angle ϕ. When ϕ is not 0 deg, the plane of incidence is rotated off the $x-z$ plane as shown in Fig. 11. To simplify the calculation procedure, we calculate the reflection and transmission coefficients in the $x'y'z'$ coordinate system for this case. The permittivity tensor in the $x'y'z'$ coordinate system can be expressed as

$$\begin{pmatrix} \varepsilon_{xx} & \varepsilon_{xy} & \varepsilon_{xz} \\ \varepsilon_{yx} & \varepsilon_{yy} & \varepsilon_{yz} \\ \varepsilon_{zx} & \varepsilon_{zy} & \varepsilon_{zz} \end{pmatrix} = \mathbf{T}_z \boldsymbol{\varepsilon} \mathbf{T}_z^{-1}, \tag{13}$$

where $\mathbf{T}_z$ is the coordinate rotational transformation matrix, and $\boldsymbol{\varepsilon}$ is the permittivity tensor of any anisotropic material in the xyz coordinate system. $\mathbf{T}_z$ is given as

$$\mathbf{T}_z = \begin{pmatrix} \cos\phi & \sin\phi & 0 \\ -\sin\phi & \cos\phi & 0 \\ 0 & 0 & 1 \end{pmatrix}. \tag{14}$$

This technique has been used by Rosa et al.[44,45] in their analysis of the Casimir interactions for anisotropic magnetodielectric metamaterials. If the incident wave is TM wave, the EM fields in the medium can be written with reference to the $x'y'z'$ coordinate system as the following form:[44]

$$\mathbf{H} = \mathbf{U}(z)\exp(j\omega t - j\beta x), \quad \text{where } \mathbf{U} = (U_x, U_y, U_z), \tag{15}$$

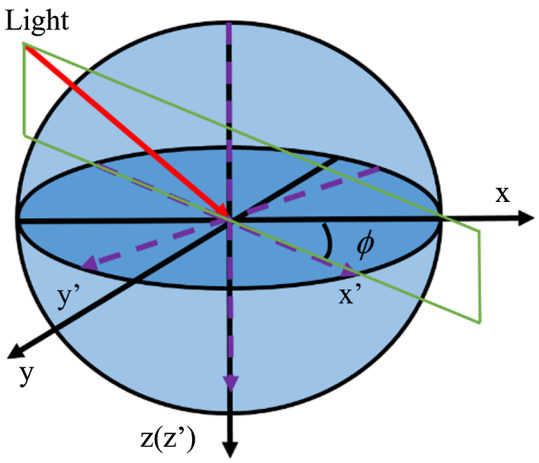

Fig. 11 Schematic of the medium and the coordinate systems in this work. The plane of incidence is tilted off the *x* axis by an angle ϕ.

$$\mathbf{E} = j(\mu_0/\varepsilon_0)^{1/2}\mathbf{S}(z)\exp(j\omega t - j\beta x), \quad \text{where } \mathbf{S} = (S_x, S_y, S_z), \tag{16}$$

where the superscript $'$ of the space variables has been dropped for brevity, and β is the wavevector component along the x-axis. The wavevector component along the z-axis is $k_z = \sqrt{k_0^2 - \beta^2}$ in vacuum. Substituting Eqs. (13), (15), and (16) into the Maxwell equations and setting $K_x = \beta/k_0$, we can get the following differential equations:

$$\frac{d}{dz}\begin{pmatrix} S_x \\ S_y \\ U_x \\ U_y \end{pmatrix} = k_0\mathbf{A}\begin{pmatrix} S_x \\ S_y \\ U_x \\ U_y \end{pmatrix}, \tag{17}$$

where the coefficient matrix as

$$\mathbf{A} = \begin{bmatrix} jK_x\varepsilon_{zx}/\varepsilon_{zz} & jK_x\varepsilon_{zy}/\varepsilon_{zz} & 0 & K_x^2/\varepsilon_{zz} - 1 \\ 0 & 0 & 1 & 0 \\ \varepsilon_{yz}\varepsilon_{zx}/\varepsilon_{zz} - \varepsilon_{yx} & \varepsilon_{yz}\varepsilon_{zy}/\varepsilon_{zz} + K_x^2 - \varepsilon_{yy} & 0 & -jK_x\varepsilon_{yz}/\varepsilon_{zz} \\ \varepsilon_{xx} - \varepsilon_{xz}\varepsilon_{zx}/\varepsilon_{zz} & \varepsilon_{xy} - \varepsilon_{xz}\varepsilon_{zy}/\varepsilon_{zz} & 0 & jK_x\varepsilon_{xz}/\varepsilon_{zz} \end{bmatrix}. \tag{18}$$

The EM fields in the medium can be described by the eigenvalues and eigenvectors of the coefficient matrix $\mathbf{A}$. We first consider a simple case that the structure consists of only one hBN slab of thickness d. The EM field vector components in the slab can be expressed as[46]

$$S_x(z) = \sum_{m=1}^{2} w_{1,m}c_m^+\exp(k_0q_mz) + \sum_{m=1}^{2} w_{1,m+2}c_m^-\exp[k_0q_m(z-d)], \tag{19}$$

$$S_y(z) = \sum_{m=1}^{2} w_{2,m}c_m^+\exp(k_0q_mz) + \sum_{m=1}^{2} w_{2,m+2}c_m^-\exp[k_0q_m(z-d)], \tag{20}$$

$$U_x(z) = \sum_{m=1}^{2} w_{3,m}c_m^+\exp(k_0q_mz) + \sum_{m=1}^{2} w_{3,m+2}c_m^-\exp[k_0q_m(z-d)], \tag{21}$$

$$U_y(z) = \sum_{m=1}^{2} w_{4,m}c_m^+\exp(k_0q_mz) + \sum_{m=1}^{2} w_{4,m+2}c_m^-\exp[k_0q_m(z-d)], \tag{22}$$

where $w_{i,m}$ is the element of the eigenvector matrix $\mathbf{W}$ of matrix $\mathbf{A}$. q_m is the eigenvalue of matrix $\mathbf{A}$, and the real parts of q_1 and q_2 are negative. c_m^+ and c_m^- are the unknowns and can be determined by applying the boundary conditions.

We calculate the reflection and transmission coefficients by matching the tangential electric and magnetic field components at the top surface of the slab as

$$\begin{pmatrix} -jk_z/k_0 \\ 0 \\ 0 \\ 1 \end{pmatrix} + \begin{pmatrix} jk_z/k_0 & 0 \\ 0 & -j \\ 0 & k_z/k_0 \\ 1 & 0 \end{pmatrix}\begin{pmatrix} r_{pp} \\ r_{ps} \end{pmatrix} = [\mathbf{W}_1 \quad \mathbf{W}_2\mathbf{X}]\begin{bmatrix} \mathbf{C}^+ \\ \mathbf{C}^- \end{bmatrix}, \tag{23}$$

and at the bottom surface of the slab as

$$[\mathbf{W}_1\mathbf{Y} \quad \mathbf{W}_2]\begin{bmatrix} \mathbf{C}^+ \\ \mathbf{C}^- \end{bmatrix} = \begin{pmatrix} -jk_z/k_0 & 0 \\ 0 & -j \\ 0 & -k_z/k_0 \\ 1 & 0 \end{pmatrix}\begin{pmatrix} t_{pp} \\ t_{ps} \end{pmatrix}, \tag{24}$$

where $\mathbf{W} = [\mathbf{W}_1 \quad \mathbf{W}_2]$ is the eigenvectors of the matrix $\mathbf{A}$. $\mathbf{C}^+$ and $\mathbf{C}^-$ are the vectors composed of the unknowns, $\mathbf{X}$ is a diagonal matrix with the diagonal elements as

$\exp(-k_0 q_m d), m = 3,4$, $\mathbf{Y}$ is a diagonal matrix with the diagonal elements as $\exp(k_0 q_m d), m = 1,2$.

Likewise, when the incident wave is a TE wave, the EM fields in the medium can be written as follows:

$$\mathbf{E} = \mathbf{S}(z)\exp(j\omega t - jk_x x), \quad \text{where } \mathbf{S} = (S_x, S_y, S_z) \tag{25}$$

and

$$\mathbf{H} = -j(\varepsilon_0/\mu_0)^{1/2}\mathbf{U}(z)\exp(j\omega t - jk_x x), \quad \text{where } \mathbf{U} = (U_x, U_y, U_z). \tag{26}$$

By substituting Eqs. (25) and (26) into the Maxwell equations, the same differential equations as those in Eq. (17) can be obtained with exactly the same coefficient matrix shown in Eq. (18). One can express the fields in the uniaxial medium in the same forms as in Eqs. (19)–(22) and apply the boundary conditions at the top and bottom surfaces of the slab, which are expressed, respectively, as

$$\begin{pmatrix} 0 \\ 1 \\ -jk_z/k_0 \\ 0 \end{pmatrix} + \begin{pmatrix} -k_z/k_0 & 0 \\ 0 & 1 \\ 0 & jk_z/k_0 \\ j & 0 \end{pmatrix} \begin{pmatrix} r_{sp} \\ r_{ss} \end{pmatrix} = [\mathbf{W}_1 \quad \mathbf{W}_2\mathbf{X}] \begin{bmatrix} \mathbf{C}^+ \\ \mathbf{C}^- \end{bmatrix} \tag{27}$$

and

$$[\mathbf{W}_1\mathbf{Y} \quad \mathbf{W}_2] \begin{bmatrix} \mathbf{C}^+ \\ \mathbf{C}^- \end{bmatrix} = \begin{pmatrix} k_z/k_0 & 0 \\ 0 & 1 \\ 0 & -jk_z/k_0 \\ j & 0 \end{pmatrix} \begin{pmatrix} t_{sp} \\ t_{ss} \end{pmatrix}. \tag{28}$$

We extend the above analysis to an arbitrary L-layer structure by matching the tangential electric and magnetic field components at each interface. Take incidence of a TM wave for an example, all the boundary conditions are

$$\begin{pmatrix} -jk_z/k_0 \\ 0 \\ 0 \\ 1 \end{pmatrix} + \begin{pmatrix} jk_z/k_0 & 0 \\ 0 & -j \\ 0 & k_z/k_0 \\ 1 & 0 \end{pmatrix} \begin{pmatrix} r_{pp} \\ r_{ps} \end{pmatrix} = [\mathbf{W}_{(1)1} \quad \mathbf{W}_{(1)2}\mathbf{X}_{(1)}] \begin{bmatrix} \mathbf{C}^+_{(1)} \\ \mathbf{C}^-_{(1)} \end{bmatrix}, \tag{29}$$

$$[\mathbf{W}_{(l-1)1}\mathbf{Y}_{(l-1)} \quad \mathbf{W}_{(l-1)2}] \begin{bmatrix} \mathbf{C}^+_{(l-1)} \\ \mathbf{C}^-_{(l-1)} \end{bmatrix} = [\mathbf{W}_{(l)1} \quad \mathbf{W}_{(l)2}\mathbf{X}_{(l)}] \begin{bmatrix} \mathbf{C}^+_{(l)} \\ \mathbf{C}^-_{(l)} \end{bmatrix} \tag{30}$$

and

$$[\mathbf{W}_{(L)1}\mathbf{Y}_{(L)} \quad \mathbf{W}_{(L)2}] \begin{bmatrix} \mathbf{C}^+_{(L)} \\ \mathbf{C}^-_{(L)} \end{bmatrix} = \begin{pmatrix} -jk_z/k_0 & 0 \\ 0 & -j \\ 0 & -k_z/k_0 \\ 1 & 0 \end{pmatrix} \begin{pmatrix} t_{pp} \\ t_{ps} \end{pmatrix}, \tag{31}$$

where $l = 2,3,\ldots,L$. $\mathbf{W}_{(l)}$, $\mathbf{X}_{(l)}$, and $\mathbf{Y}_{(l)}$ have the same definition as $\mathbf{W}$, $\mathbf{X}$, and $\mathbf{Y}$ described above. For each l, $\mathbf{W}_{(l)} = [\mathbf{W}_{(l)1} \quad \mathbf{W}_{(l)2}]$.

To preempt the numerical instability associated with the inversion of the matrix, we propose to adopt the enhanced transmittance matrix approach.[40] From Eq. (31), one has

$$\begin{bmatrix} \mathbf{C}^+_{(L)} \\ \mathbf{C}^-_{(L)} \end{bmatrix} = [\mathbf{W}_{(L)1}\mathbf{Y}_{(L)} \quad \mathbf{W}_{(L)2}]^{-1} \begin{pmatrix} \mathbf{f}_{L+1} \\ \mathbf{g}_{L+1} \end{pmatrix} \mathbf{t}, \tag{32}$$

where

$$\mathbf{t} = \begin{pmatrix} t_{pp} \\ t_{ps} \end{pmatrix}, \mathbf{f}_{L+1} = \begin{pmatrix} -jk_z/k_0 & 0 \\ 0 & -j \end{pmatrix}, \mathbf{g}_{L+1} = \begin{pmatrix} 0 & -k_z/k_0 \\ 1 & 0 \end{pmatrix}.$$

To ensure that the matrix to be inverted in Eq. (32) is numerically stable, we follow the procedure by Moharam et al.[40] and rewrite it as the product of two matrices:

$$[\mathbf{W}_{(L)1}\mathbf{Y}_{(L)} \quad \mathbf{W}_{(L)2}]^{-1} = \begin{bmatrix} \mathbf{Y}_{(L)} & 0 \\ 0 & \mathbf{I} \end{bmatrix}^{-1} [\mathbf{W}_{(L)1} \quad \mathbf{W}_{(L)2}]^{-1}. \tag{33}$$

The matrix on the right in the product is well conditioned, and its inversion is numerically stable. Therefore, Eq. (32) can be rearranged as

$$\begin{bmatrix} \mathbf{C}^+_{(L)} \\ \mathbf{C}^-_{(L)} \end{bmatrix} = \begin{bmatrix} \mathbf{Y}_{(L)} & 0 \\ 0 & \mathbf{I} \end{bmatrix}^{-1} \begin{pmatrix} \mathbf{a}_L \\ \mathbf{b}_L \end{pmatrix} \mathbf{t}, \tag{34}$$

where $\mathbf{I}$ is the unit matrix and

$$\begin{pmatrix} \mathbf{a}_L \\ \mathbf{b}_L \end{pmatrix} = [\mathbf{W}_{(L)1} \quad \mathbf{W}_{(L)2}]^{-1} \begin{pmatrix} \mathbf{f}_{L+1} \\ \mathbf{g}_{L+1} \end{pmatrix}. \tag{35}$$

We adopt the substitution $\mathbf{t} = \mathbf{a}_L^{-1}\mathbf{Y}_{(L)}\mathbf{t}_L$ such as Eq. (34) becomes

$$\begin{bmatrix} \mathbf{C}^+_{(L)} \\ \mathbf{C}^-_{(L)} \end{bmatrix} = \begin{pmatrix} \mathbf{I} \\ \mathbf{b}_L\mathbf{a}_L^{-1}\mathbf{Y}_{(L)} \end{pmatrix} \mathbf{t}_L. \tag{36}$$

Putting Eq. (36) into Eq. (30) for $l = L$, we have

$$\begin{bmatrix} \mathbf{C}^+_{(L-1)} \\ \mathbf{C}^-_{(L-1)} \end{bmatrix} = [\mathbf{W}_{(L-1)1}\mathbf{Y}_{(L-1)} \quad \mathbf{W}_{(L-1)2}]^{-1} \begin{pmatrix} \mathbf{f}_L \\ \mathbf{g}_L \end{pmatrix} \mathbf{t}_L, \tag{37}$$

where

$$\begin{pmatrix} \mathbf{f}_L \\ \mathbf{g}_L \end{pmatrix} = \mathbf{W}_{(L)1} + \mathbf{W}_{(L)2}\mathbf{X}_{(L)}\mathbf{b}_L\mathbf{a}_L^{-1}\mathbf{Y}_{(L)}. \tag{38}$$

Repeating the above process for all layers, we obtain an equation of the form

$$\begin{pmatrix} -jk_z/k_0 \\ 0 \\ 0 \\ 1 \end{pmatrix} + \begin{pmatrix} jk_z/k_0 & 0 \\ 0 & -j \\ 0 & k_z/k_0 \\ 1 & 0 \end{pmatrix} \mathbf{r} = \begin{pmatrix} \mathbf{f}_1 \\ \mathbf{g}_1 \end{pmatrix} \mathbf{t}_1, \mathbf{r} = \begin{pmatrix} r_{pp} \\ r_{ps} \end{pmatrix}. \tag{39}$$

We can solve Eq. (39) for r_{pp}, r_{ps}, and $\mathbf{t}_1$, then the transmission coefficients can be obtained as

$$\begin{pmatrix} t_{pp} \\ t_{ps} \end{pmatrix} = \mathbf{a}_L^{-1}\mathbf{Y}_{(L)}\mathbf{a}_{L-1}^{-1}\mathbf{Y}_{(L-1)}\cdots\mathbf{a}_1^{-1}\mathbf{Y}_{(1)}\mathbf{t}_1. \tag{40}$$

The process is basically the same as above for incidence of a TE wave. Hence, we can get all the reflection and transmission coefficients using the above 4×4 transfer matrix method.

Acknowledgments

This work was supported by the China Scholarship Council (No. 201706010271) for X. Wu, the National Natural Science Foundation of China (No. 51576004) for C. Fu, and the U.S. Department of Energy, Office of Science, Basic Energy Sciences (No. DE-SC0018369) for Z. M. Zhang.

References

1. Z. M. Zhang, *Nano/Microscale Heat Transfer*, McGraw-Hill, New York (2007).
2. S. Basu, Z. M. Zhang, and C. J. Fu, "Review of near-field radiation and its application to energy conversion," *Int. J. Energy Res.* **33**, 1203–1232 (2009).
3. K. Park and Z. M. Zhang, "Fundamentals and applications of near-field radiative energy transfer," *Front. Heat Mass Transfer* **4**, 013001 (2013).
4. X. L. Liu, L. P. Wang, and Z. M. Zhang, "Near-field thermal radiation: recent progress and outlook," *Nanoscale Microscale Thermophys. Eng.* **19**, 98–126 (2015).
5. C. J. Fu and W. C. Tan, "Near-field radiative heat transfer between two plane surfaces with one having a dielectric coating," *J. Quantum Spectrosc. Radiat. Transfer* **110**, 1027–1036 (2009).
6. P. B. Abdallah et al., "Near-field heat transfer mediated by surface wave hybridization between two films," *J. Appl. Phys.* **106**, 044306 (2009).
7. P. J. V. Zwol et al., "Phonon polaritons enhance near-field thermal transfer across the phase transition of VO_2," *Phys. Rev. B* **84**, 161413(R) (2011).
8. R. S. Gelais et al., "Demonstration of strong near-field radiative heat transfer between integrated nanostructures," *Nano Lett.* **14**(12), 6971–6975 (2014).
9. X. L. Liu and Z. M. Zhang, "Giant enhancement of nanoscale thermal radiation based on hyperbolic graphene plasmons," *Appl. Phys. Lett.* **107**, 143114 (2015).
10. R. Z. Zhang, X. L. Liu, and Z. M. Zhang, "Near-field radiation between graphene-covered carbon nanotube arrays," *AIP Adv.* **5**, 053501 (2015).
11. M. Laroche, R. Carminati, and J. J. Greffet, "Near-field thermophotovoltaic energy conversion," *J. Appl. Phys.* **100**, 063704 (2006).
12. R. Messina and P. B. Abdallah, "Graphene-based photovoltaic cells for near-field thermal energy conversion," *Sci. Rep.* **3**, 1383 (2013).
13. B. Zhao et al., "High-performance near-field thermophotovoltaics for waste heat recovery," *Nano Energy* **41**, 344–350 (2017).
14. L. X. Zhu, C. R. Otey, and S. H. Fan, "Ultrahigh-contrast and large-bandwidth thermal rectification in near-field electromagnetic thermal transfer between nanoparticles," *Phys. Rev. B* **88**, 184301 (2013).
15. K. F. Chen, P. Santhanam, and S. H. Fan, "Near-field enhanced negative luminescent refrigeration," *Phys. Rev. Appl.* **6**, 024014 (2016).
16. P. B. Abdallah and S. A. Biehs, "Near-field thermal transistor," *Phys. Rev. Lett.* **112**, 044301 (2014).
17. X. L. Liu and Z. M. Zhang, "Graphene-assisted near-field radiative heat transfer between corrugated polar materials," *Appl. Phys. Lett.* **104**, 251911 (2014).
18. R. Messina et al., "Graphene-based amplification and tuning of near-field radiative heat transfer between dissimilar polar materials," *Phys. Rev. B* **96**, 045402 (2017).
19. C. J. Fu and Z. M. Zhang, "Nanoscale radiation heat transfer for silicon at different doping levels," *Int. J. Heat Mass Transfer* **49**, 1703–1718 (2006).
20. X. L. Liu, R. Z. Zhang, and Z. M. Zhang, "Near-field radiative heat transfer with doped-silicon nanostructured metamaterials," *Int. J. Heat Mass Transfer* **73**, 389–398 (2014).
21. X. L. Liu, B. Zhao, and Z. M. Zhang, "Enhanced near-field thermal radiation and reduced Casimir stiction between doped-Si gratings," *Phys. Rev. A* **91**, 062510 (2015).
22. S. A. Biehs, M. Tschikin, and P. B. Abdallah, "Hyperbolic metamaterials as an analog of a blackbody in the near field," *Phys. Rev. Lett.* **109**, 104301 (2012).
23. S. A. Biehs et al., "Super-Planckian near-field thermal emission with phonon-polaritonic hyperbolic metamaterials," *Appl. Phys. Lett.* **102**, 131106 (2013).
24. X. L. Liu, R. Z. Zhang, and Z. M. Zhang, "Near-field thermal radiation between hyperbolic metamaterials: graphite and carbon nanotubes," *Appl. Phys. Lett.* **103**, 213102 (2013).
25. S. A. Biehs and P. B. Abdallah, "Near-field heat transfer between multilayer hyperbolic metamaterials," *Z. Naturforsch.* **72**(2), 115–127 (2017).
26. R. Messina et al., "Hyperbolic waveguide for long-distance transport of near-field heat flux," *Phys. Rev. B* **94**, 104301 (2016).
27. X. L. Liu and Z. M. Zhang, "Near-field thermal radiation between metasurfaces," *ACS Photonics* **2**(9), 1320–1326 (2015).

28. V. F. Hurtado et al., "Enhancing near-field radiative heat transfer with Si-based metasurfaces," *Phys. Rev. Lett.* **118**, 203901 (2017).
29. L. X. Zhu and S. H. Fan, "Persistent directional current at equilibrium in nonreciprocal many-body near field electromagnetic heat transfer," *Phys. Rev. Lett.* **117**, 134303 (2016)
30. E. M. Villa et al., "Magnetic field control of near-field radiative heat transfer and the realization of highly tunable hyperbolic thermal emitters," *Phys. Rev. B* **92**, 125418 (2015).
31. H. H. Wu, Y. Huang, and K. Y. Zhu, "Near-field radiative transfer between magneto-dielectric uniaxial anisotropic media," *Opt. Lett.* **40**(19), 4532–4535 (2015).
32. J. L. Song and Q. Cheng, "Near-field radiative heat transfer between graphene and anisotropic magneto-dielectric hyperbolic metamaterials," *Phys. Rev. B* **94**, 125419 (2016).
33. J. L. Song et al., "Three-body heat transfer between anisotropic magneto-dielectric hyperbolic metamaterials," *J. Heat Transfer* **140**(8), 082005 (2018).
34. X. L. Liu, T. J. Bright, and Z. M. Zhang, "Applications conditions of effective medium theory in near-field radiative heat transfer between multilayered metamaterials," *J. Heat Transfer* **136**(9), 092703 (2014).
35. B. Zhao et al., "Near-field transfer between graphene/hBN multilayers" *Phys. Rev. B* **95**, 245437 (2017).
36. B. Zhao and Z. M. Zhang, "Enhanced photon tunneling by surface plasmon-phonon polaritons in graphene/hBN heterostructures," *J. Heat Transfer* **139**(2), 022701 (2017).
37. K. Z. Shi, F. L. Bao, and S. L. He, "Enhanced near-field thermal radiation based on multilayer graphene-hBN heterostructures," *ACS Photonics* **4**, 971–978 (2017).
38. X. L. Liu and Y. M. Xuan, "Super-Planckian thermal radiation enabled by hyperbolic surface phonon polaritons," *Sci. China Technol. Sci.* **59**, 1680–1686 (2016).
39. P. Yeh, "Optics of anisotropic layered media: a new 4 × 4 matrix algebra," *Surf. Sci.* **96**, 41–53 (1980).
40. M. G. Moharam et al., "Stable implementation of the rigorous coupled-wave analysis for surface-relief gratings: enhanced transmittance matrix approach," *J. Opt. Soc. Am. A* **12**(5), 1077–1086 (1995).
41. R. Z. Zhang and Z. M. Zhang, "Negative refraction and self-collimation in the far infrared with aligned carbon nanotube films," *J. Quant. Spectrosc. Radiat. Transfer* **158**, 91–100 (2015).
42. J. D. Shen et al., "Super-Planckian thermal radiation enabled by coupled quasi-elliptic 2D black phosphorus plasmons," *Appl. Therm. Eng.* **144**, 403–410 (2018).
43. P. Li et al., "Optical nanoimaging of hyperbolic surface polaritons at the edges of van der Waals materials," *Nano Lett.* **17**(1), 228–235 (2017).
44. F. S. S. Rosa, D. A. R. Dalvit, and P. W. Milonni, "Casimir interactions for anisotropic magnetodielectric metamaterials," *Phys. Rev. A* **78**, 032117 (2008).
45. A. P. McCauley et al., "Structural anisotropy and orientation-induced Casimir repulsion in fluids," *Phys. Rev. A* **83**, 052503 (2011).
46. M. G. Moharam et al., "Formulation for stable and efficient implementation of the rigorous coupled-wave analysis of binary gratings," *J. Opt. Soc. Am. A* **12**(5), 1068–1076 (1995).

Xiaohu Wu received his BS degree in engineering mechanics from China University of Mining and Technology (Beijing) in 2014. Currently, he is pursuing his PhD at Peking University. He was a visiting student at Georgia Institute of Technology from Sept. 2017 to Sept. 2018. His main research interest is on thermal radiative properties of anisotropic materials and applications.

Ceji Fu received his PhD from Georgia Institute of Technology in 2004. He is now an associate professor at the Department of Mechanics and Engineering Science, Peking University, China. His main research interests include micro/nanoscale thermal radiation and non-Newtonian fluid mechanics.

Zhuomin Zhang received his PhD from Massachusetts Institute of Technology in 1992. Currently, he is a full professor in the George W. Woodruff School of Mechanical Engineering, Georgia Institute of Technology, USA. His main research interest is on micro/nanoscale thermal radiation and related applications.